UTILIZING WASTE THERMOCOL SHEETS AND RUSTED IRON WIRES TO FABRICATE CARBON–Fe_3O_4 NANOCOMPOSITE-BASED SUPERCAPACITORS: TURNING WASTES INTO VALUE-ADDED MATERIALS

Vadiyar, M. M.[1], Liu, X.[1], and Ye, Z.[1,2]*
[1] Bharti School of Engineering, Laurentian University, Sudbury, Ontario, Canada
[2] Department of Chemical and Materials Engineering, Concordia University, Montreal, Quebec, Canada
* Corresponding author (zhibin.ye@concordia.ca)

Keywords: *nanocomposite, supercapacitor*

ABSTRACT

The synthesis of porous activated carbon, Fe_3O_4 nanoparticles, and carbon–Fe_3O_4 (C@Fe_3O_4) nanocomposites from local waste thermocol sheets and rusted iron wires is demonstrated herein. The resulting carbon, Fe_3O_4 nanoparticles, and C@Fe_3O_4 composites are used as electrode materials for supercapacitor applications. In particular, C@Fe_3O_4 composite electrodes exhibit a high specific capacitance of 1375 F g^{-1} at 1 A g^{-1} and longer cyclic stability with 98% capacitance retention over 10000 cycles. Subsequently, an asymmetric supercapacitor, namely, C@Fe3O4 ‖ $Ni(OH)_2$/carbon nanotube device, exhibits a high energy density of 91.1 W h kg^{-1} and a remarkable cyclic stability, with 98% capacitance retention over 10000 cycles. Thus, this work has important implications not only for the fabrication of low-cost electrodes for high-performance supercapacitors, but also for the recycling of waste thermocol sheets and rusted iron wires for value-added reuse.

1 INTRODUCTION

Supercapacitors (SCs) have become an attractive candidate for next-generation energy-storage technologies due to their high power density, fast charging–discharging nature, and long cyclic stability compared with those of batteries.[1, 2] SCs can be classified according to their energy-storage mechanisms as either electrical double-layer capacitors (EDLCs) or pseudocapacitors.[2, 3] The energy densities of the EDLCs, in which the capacity arises from charge separation at electrode–electrolyte interfaces, are restricted for many applications.[2, 3] Pseudocapacitors, in which charge storage is achieved through Faradic redox reactions, provide significantly higher energy densities, but usually suffer from lower cyclic stability.[2, 3] Therefore, in recent decades, researchers have focused their attention towards the development of SCs with high energy density and longer cyclic stability. In this regard, asymmetric supercapacitors (ASCs), with a combination of battery-like redox electrodes and porous carbon electrodes, exhibit higher energy density because of their widened cell voltage window.[4, 5] Typical ASCs incorporate electrodes fabricated with iron-containing oxides (such as Fe_2O_3, Fe_3O_4, $ZnFe_2O_4$, and $NiFe_2O_4$) as electrode materials,[6–9] which show high capacitance and energy density values, but these metal oxides usually have poor electrical conductivity and are hydrophobic in nature.[10] Therefore, in the last few years, metal oxide nanocomposites that combine metal oxides and highly conducting carbon materials have been explored to improve electrical conductivity and energy density.[10] Synthetic carbon based materials, such as carbon nanotubes (CNTs),[11] graphene oxide,[12] graphene,[13] polymer-derived carbons,[14–16] and metal–organic framework (MOF)-derived carbon,[17] are most studied as promising electrode materials in SC applications. Activated carbons

(ACs) are, however, considered as the primary option for EDLCs, because of their low cost, high electrical conductivity, and porous nature.[18] In particular, ACs obtained from renewable natural precursors and recycled waste materials are most desired for sustainable societal developments. Hence, many experimental routes have been explored for the synthesis of high-quality ACs by using various natural precursors (such as carbons from natural biomass,[18] cotton-derived carbon,[19] popcorn-based carbon,[20] sheep manure based carbon,[21] eggshell membrane derived carbon[22]) and from wastes (e.g., waste tire derived carbon[23, 24]). However, waste thermocol sheets or foam-derived AC have not yet been reported.

With this motivation, we have synthesized, for the first time, value-added C@Fe_3O_4 hybrid nanocomposite by using the two waste materials, thermocol sheets and rusted iron wires, through wet chemical routes. The resultant C@Fe_3O_4 nanocomposite shows a high specific capacitance (1375 F g^{-1}) and high cyclic stability, with 98% retention over 10 000 cycles. In addition, all-solid-state ASCs have been constructed by using the C@Fe_3O_4 nanocomposite as the negative electrode and a high capacitance $Ni(OH)_2$/CNT composite as the positive electrode, along with a polyvinyl alcohol (PVA)–KOH gel electrolyte. Interestingly, the device has been shown to deliver a high energy density of 91.1 W h kg^{-1}, even at a very high power density of 0.8 kW kg^{-1}.

2 RESULTS AND DISCUSSION

Scheme 1 illustrates the simple protocol used herein for the synthesis of carbon, Fe3O4, and C@Fe3O4 hybrid composite, which includes acid treatment, carbonization, and the wet chemical reflux method from the two widespread waste materials, thermocol sheets and rusted iron wires.

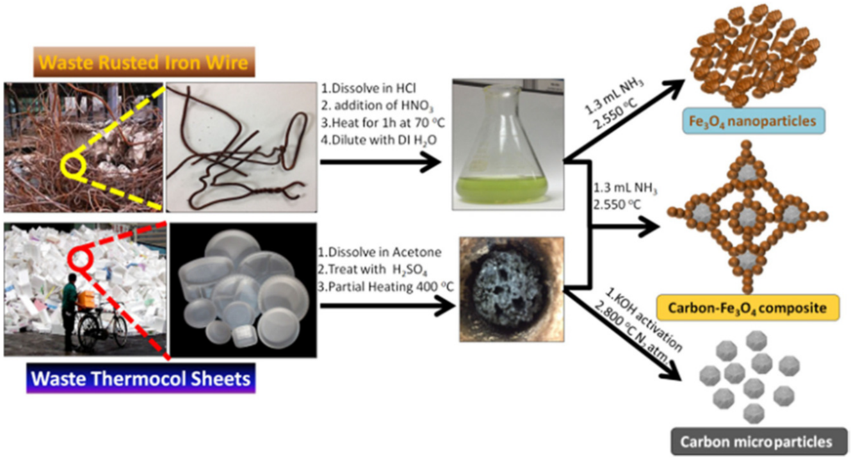

Scheme 1. Synthesis of carbon, Fe_3O_4, and C@Fe_3O_4 composite from waste thermocol and rusted iron wires.

The SEM images (Figure 1a and b) of pure Fe_3O_4 show a nanoparticle-like morphology with nanoparticles in the range of about 10–60 nm. The SEM images of pure carbon instead show microparticles with sizes of around 300 to 500 nm (Figure 1g and h). Figure 1d and e shows the SEM images of the C@Fe_3O_4 composite, in which each carbon microparticle is surrounded by small Fe_3O_4 nanoparticles without the observation of clusters of aggregated carbon microparticles; this indicates the formation of an interconnected morphology. The thermal stability of the synthesized carbon, Fe_3O_4, and C@Fe_3O_4 composite were evaluated by means of thermogravimetric analysis (TGA) in air. The TGA thermogram of pure Fe_3O_4 (Figure 2a) shows a two-step weight loss. The weight loss of about 1.8% between 35 and 130 °C corresponds to the loss of hydrated/crystallized water molecules. The weight loss of about

10.2% within the broad temperature range of 130–600 °C is ascribed to the decomposition of ammonium complex and impure phases. In comparison, the TGA thermogram of bare carbon (within 25–800 °C) shows complete weight loss between 250 and 550 °C due to the combustion of carbon in air. The TGA thermogram of the C@Fe_3O_4 hybrid composite shows a three-step weight loss (Figure 2a). A small weight loss of 0.65% within 35–150 8C is attributed to the loss of water molecules.[30] Furthermore, a weight loss of 2.5% within 150–350 8C is due to the decomposition of organic matter and ammonium complexes.[30] The last weight loss of 1.87% within 350–550 8C should correspond to the decomposition of carbonaceous matter.[31] The carbon (3.87%) and Fe_3O_4 (93.85%) contents in the C@Fe_3O_4 nanocomposite are thus calculated from the total mass loss within the temperature range of 250–550 °C. From the TGA results, the carbon to Fe_3O_4 ratio in the composite is about 1:24.

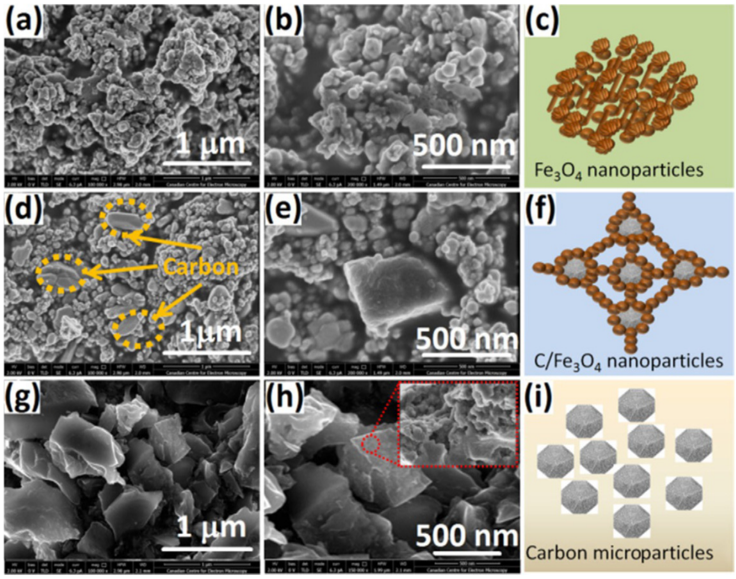

Figure 1. SEM images of Fe3O4 nanoparticles (a, b); the model structure of pure Fe3O4 nanoparticles (c); SEM images of the C@Fe3O4 hybrid composite (d, e); the model structure of the C@Fe3O4 composite (f); SEM images of pure carbon particles (g, h); the model structure of hybrid carbon particles (i).

The crystal structure and phase information of the samples were evaluated from their XRD patterns (Figure 2b). The dominant (311) peak at 2θ=35.5°, along with other lower intensity peaks ((111), (220), (400), (422), (511) and (440) at 2 θ =18.2, 30.1, 43.9, 54.2, 58.6, and 63.2°, respectively), are observed in both the Fe_3O_4 and C@Fe_3O_4 samples, which are characteristic of the cubic spinel phase of Fe_3O_4 nanoparticles.[32] There is no significant peak of graphitic carbon at 2θ =25.5° in the C@Fe_3O_4 composite, which indicates the primary amorphous disordered structure of the carbon microparticles.[32] The XRD pattern is agreement with JCPDS card no. 01-075-0449 (for Fe_3O_4), as shown in Figure 2b. For comparison, in the XRD pattern of the pure carbon, there is only a weak, broad peak centered at around at 25.0°, which supports the predominantly amorphous nature of carbon. Figure 2c shows comparative Raman spectra of pure Fe_3O_4, carbon, and the C@Fe_3O_4 composite. The Raman spectrum (Figure 2c) of pure Fe3O4 shows various vibrational modes within the wavenumber range of 200–700 cm^{-1}, which confirms the formation of the spinel cubic phase.[31] In particular, bands above 600 cm^{-1} (606 and 664 cm^{-1}) correspond to the vibrations of Fe^{2+}–O (FeO_4 units) in tetrahedral sites, which have $2A_{1g}$ symmetry.[31] The other bands at 272, 292, 401, and 501 cm^{-1} are due to the vibrations of Fe^{3+}–O (FeO_6 units) in octahedral sites, which are considered to have $3T_{2g}$ and E_g

symmetry. On other hand, the Raman spectrum of the C@Fe_3O_4 composite reveals that, along with Fe_3O_4 vibrational modes, an additional broad band appears at 1298 cm^{-1}, which is attributed to amorphous carbon.[31] The difference in the carbon Raman bands of the pure carbon and C@Fe_3O_4 composite is because of double carbonization. Initially, pure carbon was obtained from the carbonization of partially oxidized carbon, with KOH as an activating agent at 800 °C for 1 h. This resulted in amorphous carbon, which was further used for the synthesis of the C@Fe_3O_4 composite. During synthesis of the composite, the C@Fe–OH composite was annealed at 500 °C for 5 h. The annealing treatment resulted in the new amorphous carbon band at 1298 cm^{-1}, at which typical D and G bands of carbon significantly overlap.[31]

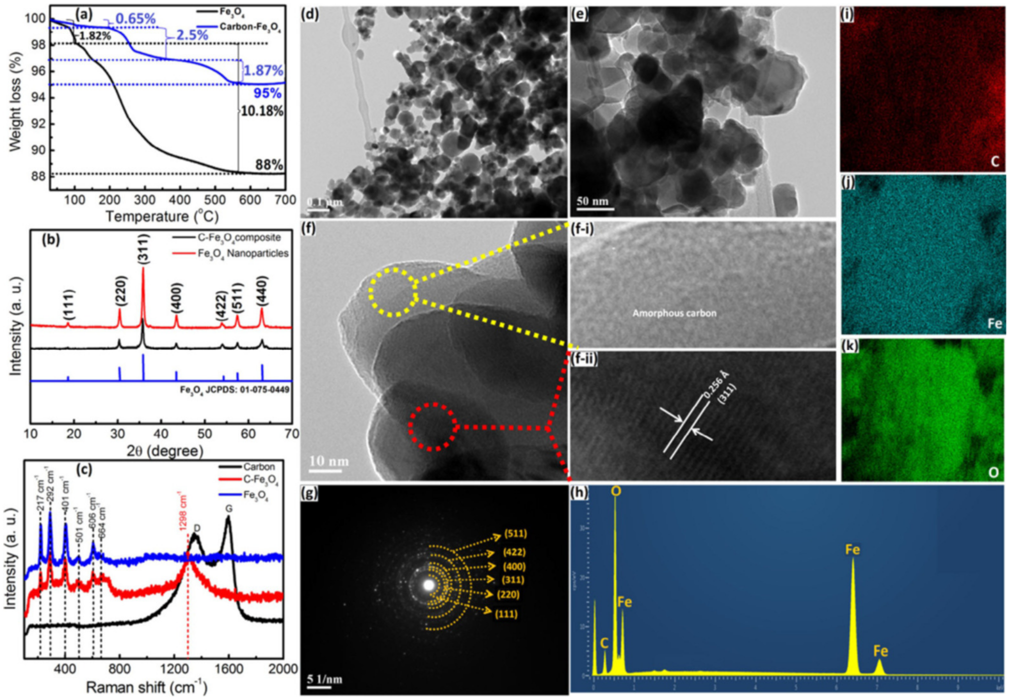

Figure 2. a) TGA thermograms and b) XRD patterns of Fe_3O_4 and the C@Fe_3O_4 composite. c) Raman spectra of carbon, Fe_3O_4, and the C@Fe_3O_4 composite. TEM images (d, e), high-resolution (HR) TEM images (f), and selected-area electron diffraction (SAED) pattern (g) of the C@Fe_3O_4 composite. h) Energy-dispersive X-ray spectroscopy (EDS) pattern of the C@Fe_3O_4 composite. Elemental mapping of C (i), Fe (j), and O (k) in the C@Fe_3O_4 composite (from SEM imaging).

Figure 2d and e shows the low-magnification TEM images of the C@Fe_3O_4 composite, and Figure 2f, f-i, and f-ii shows the HRTEM images. The HRTEM images show two distinct parts corresponding to amorphous carbon (Figure 2f-i) and crystalline Fe_3O_4 nanoparticles (Figure 2f–ii).[32] The HRTEM image of Fe_3O_4 (Figure 2f-ii) shows lattice fringes, with an interplanar distance 2.56 Å, corresponding to the (311) plane of the cubic spinel phase.[32] The SAED pattern (Figure 2g) exhibits a set of diffraction rings with some scattered dots; this is indicative of the crystalline nature, but with the long-range disorder of Fe_3O_4. The diffraction rings can be readily indexed to the (111), (220), (311), (400), (422), and (511) planes of the spinel cubic Fe_3O_4, which are in good agreement with the XRD results (Figure 2b).[32] EDS and elemental mapping were used to characterize the chemical composition and elemental distribution in the C@Fe_3O_4 composite. The EDS results (Figure 2h) confirm the existence of C, Fe, and O elements.[33] As shown in Figure 2i–k, elemental mapping (from SEM imaging) demonstrates that C, Fe, and O elements are all distributed uniformly.[33] This confirms that carbon particles and Fe_3O_4 nanoparticles are uniformly distributed within the composite.

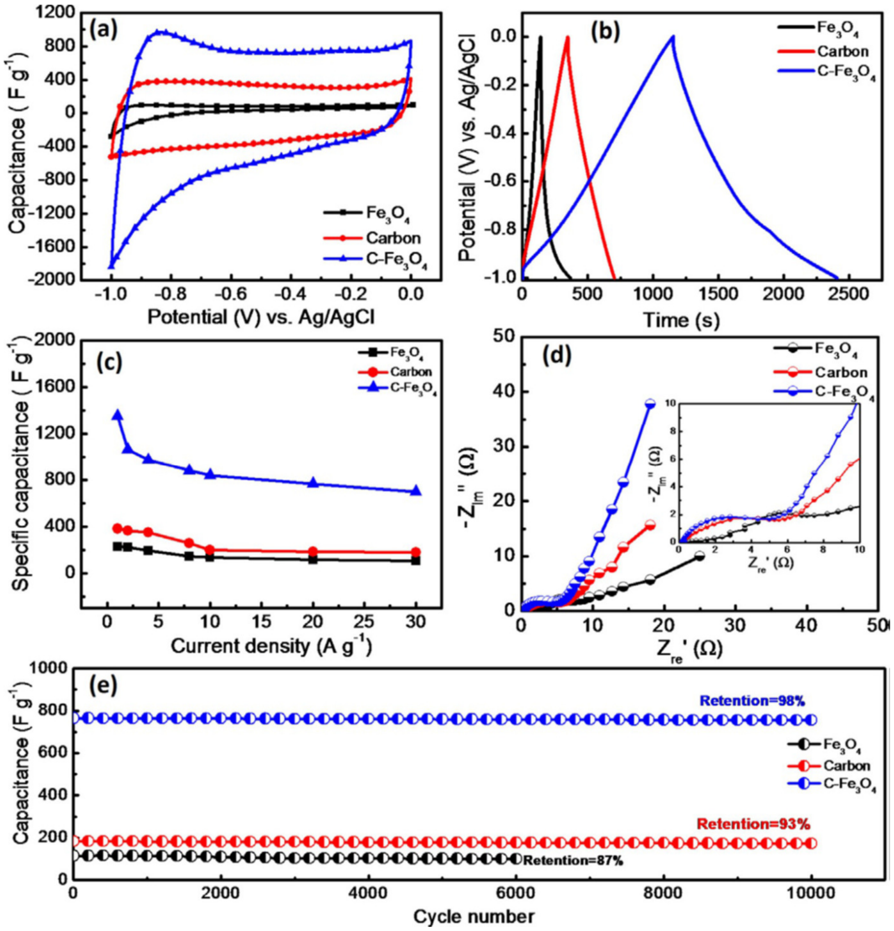

Figure 3. a) CV curves at a scan rate of 10 mV s^{-1}. b) GCD curves at 1 A g^{-1}. c) Plots of specific capacitance versus current density. d) Nyquist plots (inset shows high-resolution Nyquist plots). e) Cyclic stability curves (over 10000 cycles at 20 A g^{-1}) of carbon, pure Fe_3O_4, and the Fe_3O_4 composite active materials.

Supercapacitive properties of the synthesized carbon, Fe_3O_4, and C@Fe_3O_4 composite were evaluated in a three-electrode cell in 6 M KOH electrolyte. Initially, to optimize the carbon and Fe_3O_4 content in the composite for the best capacitive performance, we prepared three different composites by using various carbon feed amounts (0.01, 0.02, and 0.03 g) with respect to the same volume (30 mL) of standard Fe^{3+} precursor solution during the composite synthesis. The cyclic voltammetry (CV) and galvanostatic charge–discharge (GCD) performances of the various electrodes have been evaluated. The composite prepared with 0.02 g of carbon displays the highest capacitance, and hence, it is used throughout this study. The comparative CV curves of the carbon, Fe_3O_4, and C@Fe_3O_4 samples at a scan rate of 10 mV s^{-1} are presented in Figure 3a. The C@Fe_3O_4 composite exhibits a CV curve of a distorted rectangular shape, which indicates that both the pseudocapacitance (Fe^{3+}/Fe^{2+}/Fe^0 redox reactions)[31, 38] and electrical double-layer capacitance contribute to energy storage. On the contrary, pure Fe_3O_4 and pure carbon show purely pseudocapacitance (Fe^{3+}/Fe^{2+}/Fe^0 redox reactions)[38] and purely electrical double-layer capacitance, respectively, as shown in Figure 3a. The area under the CV curve of the C@Fe_3O_4 composite shows a much higher capacitance (1015 F g^{-1}) than those of pure Fe_3O_4 (156 F g^{-1}) and pure carbon (336 F g^{-1}) as active materials. The large capacitance of the C@Fe_3O_4 composite is ascribed to the optimized composition, interconnected morphology between the carbon and Fe_3O_4 particles, and improved electrical conductivity, which contributes to the efficient use of the pseudocapacitance of the Fe_3O_4 nanoparticles.

The capacitive behavior of the C@Fe_3O_4 composite can also be proven by its triangle-like GCD curves (Figure 3b).[31] The small asymmetry is caused by the pseudocapacitance of Fe_3O_4. The specific capacitance of the C@Fe_3O_4 composite, calculated from the GCD results, is 1375 F g^{-1} at a current density of 1 A g^{-1} (Figure 3c). This value is six and three times greater than the values of pure Fe_3O_4 (230 F g^{-1}) and pure carbon (382 F g^{-1}), respectively, at the same current density. This is in good agreement with the specific capacitance obtained from CV measurements. The ability to store/deliver energy at high current densities is the most advantageous property of SCs over that of batteries. Due to its hierarchical porous structure, which facilitates fast electrolytic ion transfer and strong interconnected morphology, the C@Fe_3O_4 composite shows a high specific capacitance of 697 F g^{-1}, even at a higher current density of 30 A g^{-1}; this indicates its high rate performance. Pure Fe_3O_4 and pure carbon instead show only capacitances of 108 and 180 F g^{-1}, respectively, at 30 A g^{-1} (Figure 3c).

Furthermore, fast ion transfer in the C@Fe_3O_4 composite electrode can be confirmed by Nyquists plots (Figure 3d) recorded from 0.01 to 50000 Hz at open-circuit potential. The C@Fe_3O_4 composite electrode exhibits a small equivalent series resistance (ESR; 0.15 W) and smaller semicircle, that is, charge transfer resistance (R_{ct}; 4.7 W).[8] In addition, it has a smaller Warburg resistance (R_w; 4.2 W) and a Warburg line with a much higher slope, which indicates fast ion transfer.[8] The highest frequency, namely, the starting point, of the Warburg line for the C@Fe_3O_4 composite electrode is 50 Hz, which is significantly higher than those of pure Fe_3O_4 (5.5 Hz) and pure carbon (9.0 Hz); this indicates excellent capacitive response of the C@Fe_3O_4 composite electrode.[33] The cyclic life of the C@Fe_3O_4 composite electrode was also studied at a high current load (20 A g^{-1}; Figure 3e). After 10 000 GCD cycles, the capacitance loss is only 2%. It thus proves that the C@Fe_3O_4 composite electrode has excellent cyclic life because of the strongly interconnected morphology, with homogeneous spreading of Fe_3O_4 nanoparticles over the microporous carbon particles. The durability of the C@Fe_3O_4 composite electrode in cycling is marginally higher than those of electrodes of pure Fe_3O_4 (13% loss after 6000 cycles) and pure carbon (7% loss after 10000 cycles).

To evaluate the performance of each electrode as the negative electrode in actual devices, three all-solid-state ASCs were constructed with the $Ni(OH)_2$–CNT electrode as the positive electrode with PVA–KOH gel electrolyte. Given their different specific capacitances and voltage ranges, the active mass loading of the positive electrodes was matched according to the active mass of the negative electrode. Hence, mass loadings of 0.18, 0.35, and 0.55 mg of $Ni(OH)_2$–CNT were balanced with respect to the pure Fe_3O_4 (1.4 mg), pure carbon (1.9 mg), and C@Fe_3O_4 (1.8 mg) negative electrodes, respectively. Scheme 2a illustrates a schematic diagram of the C@Fe_3O_4 ‖ $Ni(OH)_2$/CNT ASC device, with photographs of the actual electrodes and device shown in Scheme 2b and c, respectively.

The CV curves of the three pairs of negative and positive electrodes are presented in Figure 4a at a scan rate of 10 mV s^{-1}; these results reveal that the cell voltage is operable up to 1.6 V. Furthermore, the voltage range of the full ASC cell (C@Fe3O4 ‖ Ni(OH)2/CNT) was evaluated by recording CV curves at various voltage ranges (0.4, 0.8, 1.0, 1.2, 1.4, and 1.6 V) at a constant scan rate of 30 mV s^{-1} (Figure 4b). The ASC device is able to operate in the cell voltage range of 1.6 V with negligible polarization. As such, CV curves of the C@Fe3O4 ‖ Ni(OH)2/CNT device were collected at various scan rates (10–100 mV s^{-1}) within 0–1.6 V (Figure 4c), in which the shapes of the CV curves are well maintained, even at a higher scan rate of 100 mV s^{-1}, which indicates the desired high rate performance. The area within the CV curves of the C@Fe_3O_4 ‖ $Ni(OH)_2$/CNT device is much higher than those of the other two ASC devices; this indicates its significantly higher capacitance.

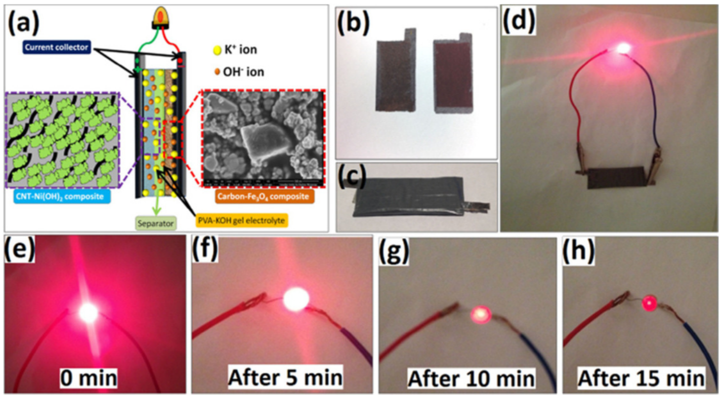

Scheme 2. a) Illustration of the C@Fe₃O₄ ‖ Ni(OH)₂CNT ASC device. Photographs of b) the actual 2 cm × 1 cm Ni(OH)₂–CNT and C@Fe₃O₄ electrodes; c) the actual assembled ASC device; d) the actual ASC device lighting up a red light-emitting diode (LED) bulb; and of discharging of the LED after 0 (e), 5 (f), 10 (g), and 15 min (h).

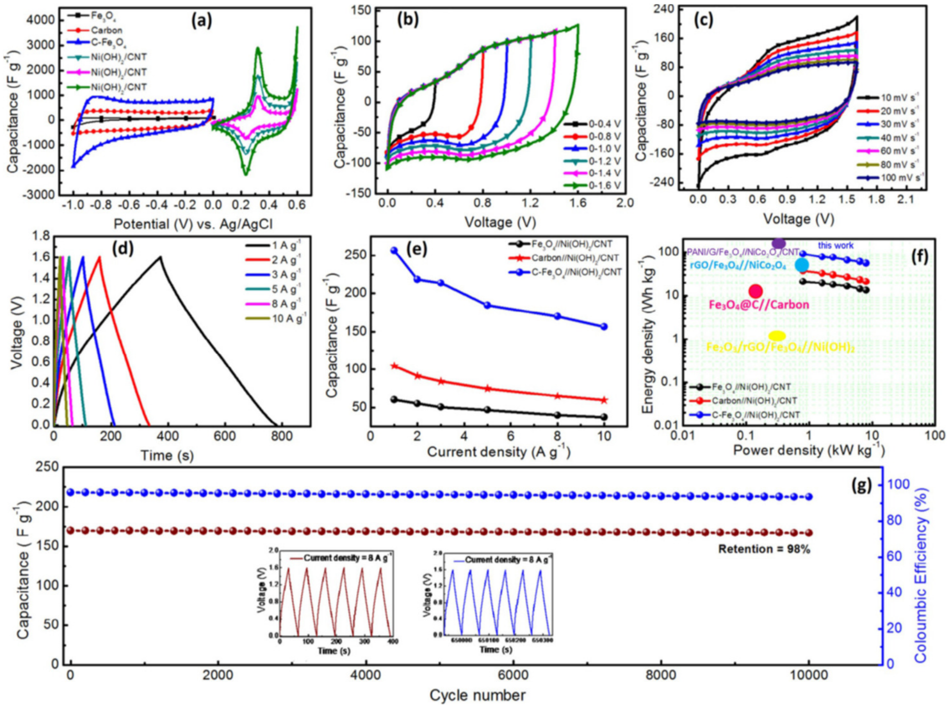

Figure 4. a) CV curves of individual electrodes that incorporate pure Fe₃O₄, pure carbon, and the C@Fe₃O₄ composites, with respect to the Ni(OH)₂/CNT electrode within the voltage range of @1 to 0.6 V at a scan rate of 10 mV s^{-1}. b) CV curves within different voltage windows. c) CV curves at various scan rates of 10–100 mV s^{-1} within 1.6 V. d) GCD curves at various current densities. e) Plot of specific capacitance versus current density. f) A Ragone plot. g) Cyclic stability over 10000 cycles at 8 A g^{-1} (insets: first (up to 400 s) and last six cycles (from 650 000 s to 650300 s)) of the solid-state asymmetric C@Fe₃O₄ ‖ Ni(OH)₂/CNT device.

In addition, GCD curves of the C@Fe_3O_4 ‖ $Ni(OH)_2$/CNT device at various current densities (1–10 A g^{-1}) are presented in Figure 4d. The device shows curves of a quasi-triangular-type shape, which implies that the electrochemical reaction is highly reversible, even at a high current density of 10 A g^{-1}. For comparison, the Fe_3O_4 ‖ $Ni(OH)_2$/CNT and carbon ‖ $Ni(OH)_2$/CNT ASC devices display GCD curves of a distorted triangular shape, with smaller discharging times at the same current densities as those of the former device; this indicates lower specific capacitance values. The calculated specific capacitances of all three devices are shown and compared in Figure 4e. The C@Fe_3O_4 ‖ $Ni(OH)_2$/CNT device shows a high specific capacitance of 256 F g^{-1} at 1 A g^{-1}, which is much higher than those of the Fe_3O_4 ‖ $Ni(OH)_2$/CNT (60 F g^{-1}) and carbon ‖ $Ni(OH)_2$/CNT (104 F g^{-1}) devices at the same current. This specific capacitance value (256 F g^{-1} at 1 A g^{-1}) is also higher than that of many values reported in the literature on similar ASCs incorporating iron oxides or their composites as the active materials. Moreover, the C@Fe_3O_4 ‖ $Ni(OH)_2$/CNT device retains a specific capacitance of 156 F g^{-1}, even at 10 A g^{-1}, as shown in Figure 4e, which represents 60% retention relative to that at 1 A g^{-1}. The improved capacitance and retention are attributed to high electrical conductivity and fast ion intercalation–deintercalation into the porous structures.

Energy density and power density are two key factors for SC devices. The corresponding Ragone plots for the three ASC devices are shown in Figure 4f. Impressively, the C@Fe_3O_4 ‖ $Ni(OH)_2$/CNT device delivers a ultrahigh energy density of 91.1 W h kg^{-1} at a power density of 0.8 kW kg^{-1} within the voltage window of 1.6 V, and still maintains an energy density of 55 W h kg^{-1}, even at a very high power density of 8.0 kW kg^{-1}. These results are much higher than those of similar ASCs reported recently. [33, 42-46] The cyclic stability of the C@Fe_3O_4 ‖ $Ni(OH)_2$/CNT device was performed at a high current density of 8 A g^{-1} over 10000 cycles (Figure 4g). After 10000 cycles, the device retains 98% of its initial capacitance, which indicates excellent cyclic stability. The insets of Figure 4g show the first and last six GCD cycles. The assembled C@Fe_3O_4 ‖ $Ni(OH)_2$/CNT ASC device was used in a real application to illuminate a 1.8 V red LED bulb over 15 min (Scheme 2d–h). The discharging ability of the red LED bulb was captured in the form of actual photographs (Scheme 2e–h) taken at various times between 0 and 15 min. The work reported herein thus not only demonstrates that waste thermocol sheets and waste rusted iron wires can find value-added reuse as alternative high-performance electrode materials for SC devices, but also provides a successful approach for the recycling/reuse of the two waste materials.

3 CONCLUSIONS

The fabrication of high-performance C-Fe_3O_4 composite supercapacitor electrode is demonstrated by using low-cost waste thermocol sheets and rusted iron wires. In particular, microporous activated carbon with the high surface area (1,883 m^2 g^{-1}) is obtained from the thermocol sheets. A C-Fe_3O_4 composite, with strongly interconnected Fe_3O_4 nanoparticles on the carbon microparticles, has been synthesized via a simple reflux precipitation approach. Benefiting from the high surface area and high electrical conductivity of the carbon and the high pseudocapacitance of the interconnected Fe_3O_4 nanoparticles, high capacitance, a high long cyclic stability C-Fe_3O_4 composite electrode has been obtained. Furthermore, an all-solid-state asymmetric supercapacitor device, (C-Fe_3O_4 ‖ $Ni(OH)_2$/CNT, has been constructed. The device exhibits ultrahigh energy density of 91.1 Wh kg^{-1} at power density of 0.8 kW kg^{-1}. It also shows an excellent cyclic stability with 98% of capacity retention over 10,000 cycles. Finally, the work demonstrates an alternative way to the convenient recycling of abundant waste thermocol sheets and rusted iron wires for the development of low-cost, value-added, high-performance electrodes for electrochemical energy storage applications.

4 REFERENCES

This paper is adapted from a published one (Vadiyar, M. M., Xu, D. and Ye, Z. Utilizing waste thermolcol sheets and rusted iron wires to fabricate carbon-Fe_3O_4 nanocompostie based supercapacitors: turning wastes into value-added materials. *ChemSusChem*, Vol. 11, No. 14, pp 2410-2420, 2018) by the same authors for the purpose of oral presentation at CANCOM 2022 conference. The references cited herein follow exactly the list in the published paper. Please refer to the published paper for the detailed references, as well as the experimental procedures.